Applied Physics Letters

Nonreciprocity and isolation induced by an angular momentum bias in convection-diffusion systems

Cite as: Appl. Phys. Lett. **118**, 221902 (2021); https://doi.org/10.1063/5.0049774
Submitted: 09 March 2021 . Accepted: 19 May 2021 . Published Online: 02 June 2021

Liujun Xu, Jiping Huang, and Xiaoping Ouyang

AIP Publishing

Applied Physics Letters ARTICLE scitation.org/journal/apl

Nonreciprocity and isolation induced by an angular momentum bias in convection-diffusion systems

Cite as: Appl. Phys. Lett. **118**, 221902 (2021); doi: 10.1063/5.0049774
Submitted: 9 March 2021 · Accepted: 19 May 2021 ·
Published Online: 2 June 2021

Liujun Xu,[1,a)] Jiping Huang,[1,a)] and Xiaoping Ouyang[2,a)]

AFFILIATIONS

[1]Department of Physics, State Key Laboratory of Surface Physics, and Key Laboratory of Micro and Nano Photonic Structures (MOE), Fudan University, Shanghai 200438, China
[2]School of Materials Science and Engineering, Xiangtan University, Xiangtan 411105, China

[a)]**Authors to whom correspondence should be addressed:** 13307110076@fudan.edu.cn; jphuang@fudan.edu.cn; and oyxp2003@aliyun.com

ABSTRACT

Inspired by the electronic and acoustic Zeeman effects in wave systems, we demonstrate here that an angular momentum bias generated by a volume force can also lead to modal splitting in convection-diffusion systems but with different features. We further reveal the thermal Zeeman effect by studying the temperature propagation in an angular-momentum-biased ring with three ports (one for input and two for output). In the presence of an optimal volume force, temperature propagation is allowed at one output port but isolated at the other, so rectification coefficient can reach a maximum value of 1. The volume forces corresponding to rectification coefficient peaks can also be predicted by scalar (i.e., temperature) interference quantitatively. Compared with existing mechanisms of thermal nonreciprocity, an angular momentum bias does not require temperature-dependent and phase-change materials, which has an advantage in wide-temperature-range applicability. These results may provide insights into thermal stabilization and thermal topology. The related mechanism is also general for other convection-diffusion systems such as mass transport, chemical mixing, and colloid aggregation.

Nonreciprocity refers to asymmetric propagation along different directions, which has aroused broad interest in wave systems.[1,2] A common approach to nonreciprocity is based on the modal splitting induced by an angular momentum bias. For example, electromagnetic nonreciprocity can be realized in magneto-optical media based on the electronic Zeeman effect. Inspired by the electronic Zeeman effect, the acoustic Zeeman effect was also proposed to obtain acoustic nonreciprocity with air circulation.[3] The origin of an angular momentum bias is various, which can be attributed to circular motions,[3,4] magnetic fields,[5,6] or spatiotemporal modulations.[7–10] However, the related mechanism is confronted with many challenges in convection-diffusion systems. On the one hand, it is unknown how to apply an angular momentum bias in convection-diffusion systems. On the other hand, convection-diffusion systems have many crucial differences from wave systems, which are discussed in detail when exhibiting our results.

Macroscopic thermal transport is a typical convection-diffusion system, where breaking reciprocity is highly expected and widely explored.[11] Reciprocity generally refers to that a physical quantity has the same properties along different directions. For thermal transport, the physical quantity can be heat flux, temperature amplitude, etc. Thermal nonreciprocity can be realized with temperature-dependent (i.e., nonlinear) or phase-change materials,[12–14] but the strong dependence on temperature restricts its wide-temperature-range applicability. Moreover, spatiotemporal modulations can also help to achieve thermal nonreciprocity,[15,16] but thermal conductivities and mass densities require complicated and dynamic control. Therefore, it remains difficult to realize thermal nonreciprocity with linear, wide-temperature-range applicable, and easy-to-control materials.

Inspired by the electronic and acoustic Zeeman effects in wave systems,[3–10] we introduce the thermal Zeeman effect with an angular momentum bias generated by a volume force [see Figs. 1(a) and 1(b)]. Here, a volume force is a force exerted on all fluid particles and is proportional to the mass of the fluid in that volume, such as the forces exerted on fluids in a gravitational field and ferrofluids in a magnetic field. We then study the temperature propagation in a three-port ring

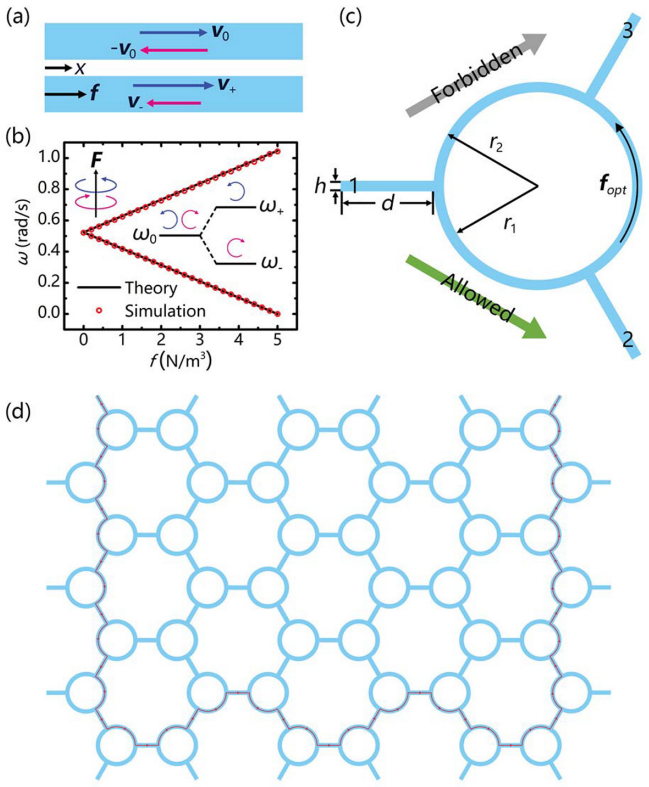

FIG. 1. The thermal Zeeman effect. (a) Schematic diagram of modal splitting. (b) Splitting of the real part of frequency as a function of volume force. (c) Angular-momentum-biased ring exhibiting thermal nonreciprocity and isolation. (d) Schematic diagram of thermal topology.

to achieve thermal nonreciprocity and isolation [see Fig. 1(c)]. Here, temperature propagation refers to the propagation of a periodic temperature profile,[17–25] which can also be regarded as a temperature fluctuation. Scalar (i.e., temperature) interference is crucial to explain thermal nonreciprocity, which quantitatively predicts the rectification coefficient peaks found in simulations. The present scheme is free from nonlinear and phase-change materials, so it is applicable to a wide temperature range. Moreover, complicated control of parameters is also not necessary, which is feasible in practice. Following the idea that acoustic topology can be achieved by arranging three-port rings in a graphene-like array,[26–31] we may also realize thermal topology with the proposed mechanism of thermal nonreciprocity [see Fig. 1(d)].

Let us start from the thermal Zeeman effect. A thermal convection-diffusion process is dominated by $\rho C\partial T/\partial t + \nabla\cdot(-\kappa\nabla T + \rho C\boldsymbol{v}T) = 0$, where ρ, C, κ, and $\boldsymbol{v}$ are the mass density, heat capacity, thermal conductivity, and convective velocity of a fluid, respectively.[32] T and t represent absolute temperature and time, respectively. Without loss of generality, we discuss a steady incompressible creeping flow[33–36] driven by a linear pressure field along the x axis. A convective velocity $\boldsymbol{v}(y)$ has a quadratic distribution along the vertical direction.[37] We consider a small vertical height h and discuss an average convective velocity $\boldsymbol{v} = -h^2(\nabla P - \boldsymbol{f})/(12\mu)$, where μ is the dynamic viscosity of the fluid, P denotes pressure, and $\boldsymbol{f}$ is the volume force.[37] In what follows, we also discuss the average values of velocities, temperatures, and heat fluxes.

We then consider a periodic temperature profile $T = A\cos(\beta x - \omega t) + T_0$, where A, β, ω, and T_0 are temperature amplitude, wave number, circular frequency, and reference temperature, respectively. In the absence of a volume force $\boldsymbol{f}$, a pressure field along $+x$ (or $-x$) generates an average convective velocity $\boldsymbol{v}_0$ (or $-\boldsymbol{v}_0$), see the upper inset of Fig. 1(a). Therefore, circular frequencies are the same, i.e., $\omega_0 = \beta v_0 - \mathrm{i}\beta^2 D$ with thermal diffusivity $D = \kappa/(\rho C)$. $\mathrm{Re}(\omega_0)$ represents circular frequency, and $-\mathrm{Im}(\omega_0)$ denotes temporal decay rate. When there is a volume force $\boldsymbol{f}$ along $+x$, a pressure field along $+x$ (or $-x$) generates an average convective velocity $\boldsymbol{v}_+$ (or $\boldsymbol{v}_-$), see the lower inset of Fig. 1(a). Circular frequencies are no longer the same but split into

$$\omega_\pm = \beta v_\pm - \mathrm{i}\beta^2 D, \tag{1}$$

with $v_\pm = v_0 \pm h^2 f/(12\mu)$. The difference between convection-diffusion systems and wave systems is reflected on the imaginary part of Eq. (1). Wave systems are generally Hermitian with energy conservation, so circular frequencies are real numbers without loss.[3] However, convection-diffusion systems are non-Hermitian with loss,[19] so circular frequencies become complex.

For intuitive understanding, we can imagine periodic conditions on the left and right boundaries in Fig. 1(a) and regard the $+x$ direction as the anticlockwise azimuthal direction. An angular velocity $\boldsymbol{V} = \boldsymbol{e}_r \times \boldsymbol{v}/r_0$ and an angular volume force $\boldsymbol{F} = \boldsymbol{e}_r \times \boldsymbol{f}/r_0$ are introduced, where $\boldsymbol{e}_r$ is the radial unit vector and r_0 is an average radius. The ring allows only discrete wave numbers, i.e., $\beta = N/r_0$, where N is a positive integer.[19] The frequency splitting described in Eq. (1) can then be understood by the Zeeman effect, which results from an angular momentum bias generated by an angular volume force $\boldsymbol{F}$, just like the energy splitting of atoms due to a magnetic bias or the frequency splitting of sounds due to an angular momentum bias.[3] We also confirm the frequency splitting with finite-element simulations based on the template of *Heat Transfer in Fluids* in COMSOL Multiphysics (http://www.comsol.com/). Meshes are set as following: the maximum element size is 5×10^{-4} m, the minimum element size is 10^{-6} m, the maximum element growth rate is 1.1, the curvature factor is 0.2, and the resolution of narrow regions is 1. The relative tolerance for time-dependent solver is 10^{-4}. We use the parameters of water that is a common material of broad applications like water-cooling. We also set a pressure gradient of $|\nabla P| = 5\,\mathrm{N/m^3}$, a wave number of $\beta = 100\pi\,\mathrm{m}^{-1}$, and a height of $h = 2$ mm. The real part of Eq. (1) then becomes $\omega_\pm = \pi(5\pm f)/30$. The simulation result agrees well with the theory [see Fig. 1(b)].

To demonstrate thermal nonreciprocity with the thermal Zeeman effect, we further consider a three-port ring, as shown in Fig. 1(c). We set port 1 to be an input port and ports 2 and 3 to be output ports. We set a high pressure P_h at port 1 and two identical low pressures P_l at ports 2 and 3. We also set a periodic temperature source at port 1, i.e., $T_1 = A_1\cos(-\omega t) + T_0$. Ports 2 and 3 are set with open conditions with no reflection. For a zero volume force, two symmetrical velocities are obtained in the ring, i.e., $v_{1\to2}$ along the counterclockwise direction and $v_{1\to3}$ along the clockwise direction. Therefore, temperature propagation at ports 2 and 3 are identical due to structural symmetry. However, when a volume force along the

counterclockwise direction is applied, $v_{1\to2}$ increases but $v_{1\to3}$ decreases. Therefore, an angular momentum bias is achieved in the ring, and the temperature propagation from port 1 to port 3 is forbidden with an optimal volume force f_{opt}.

We then perform finite-element simulations with time steps of 0.5 s to observe thermal nonreciprocity. Two crucial parameters should be considered, i.e., the Peclet number and the Reynolds number. Since we use water for simulations, the Peclet number is Pe = 2800, demonstrating that convection is dominant. As a result, the convection-diffusion equation mainly exhibits hyperbolic features that can support the propagation of wave-like temperature profiles. The Reynolds number is Re = 4 that approximately corresponds to a creeping or laminar flow,[33–36] so the effects of boundary layer behavior and singular perturbation can be ignored. In short terms, the expected phenomena require (I) a large Peclet number for convection ≫ diffusion and (II) a small Reynolds number without turbulent flow.

The properties of temperature propagation can be reflected on temperature amplitudes. A zero temperature amplitude indicates that temperature propagation is isolated. The temperature and velocity profiles without a volume force are shown in the first column of Fig. 2. The temperature amplitudes at ports 2 and 3 are identical due to structural symmetry. However, it is crucially different when the volume force reaches an optimal value $f_{opt} = 2\,\mathrm{N/m^3}$. The temperature amplitude at port 3 is dramatically reduced to zero, whereas that at port 2 still exists (see the second column in Fig. 2). In other words, we achieve the isolation of temperature propagation at port 3, and thermal nonreciprocity is maximized. We then continue to increase the volume force to $6\,\mathrm{N/m^3}$. Although nonreciprocity still exists (see the third column in Fig. 2), the temperature amplitude at port 3 is no longer zero. The velocity profiles with different volume forces are shown in Figs. 2(g)–2(i). The velocities at three ports are irrelevant to the volume force, but those in the ring are affected linearly for realizing an angular momentum bias.

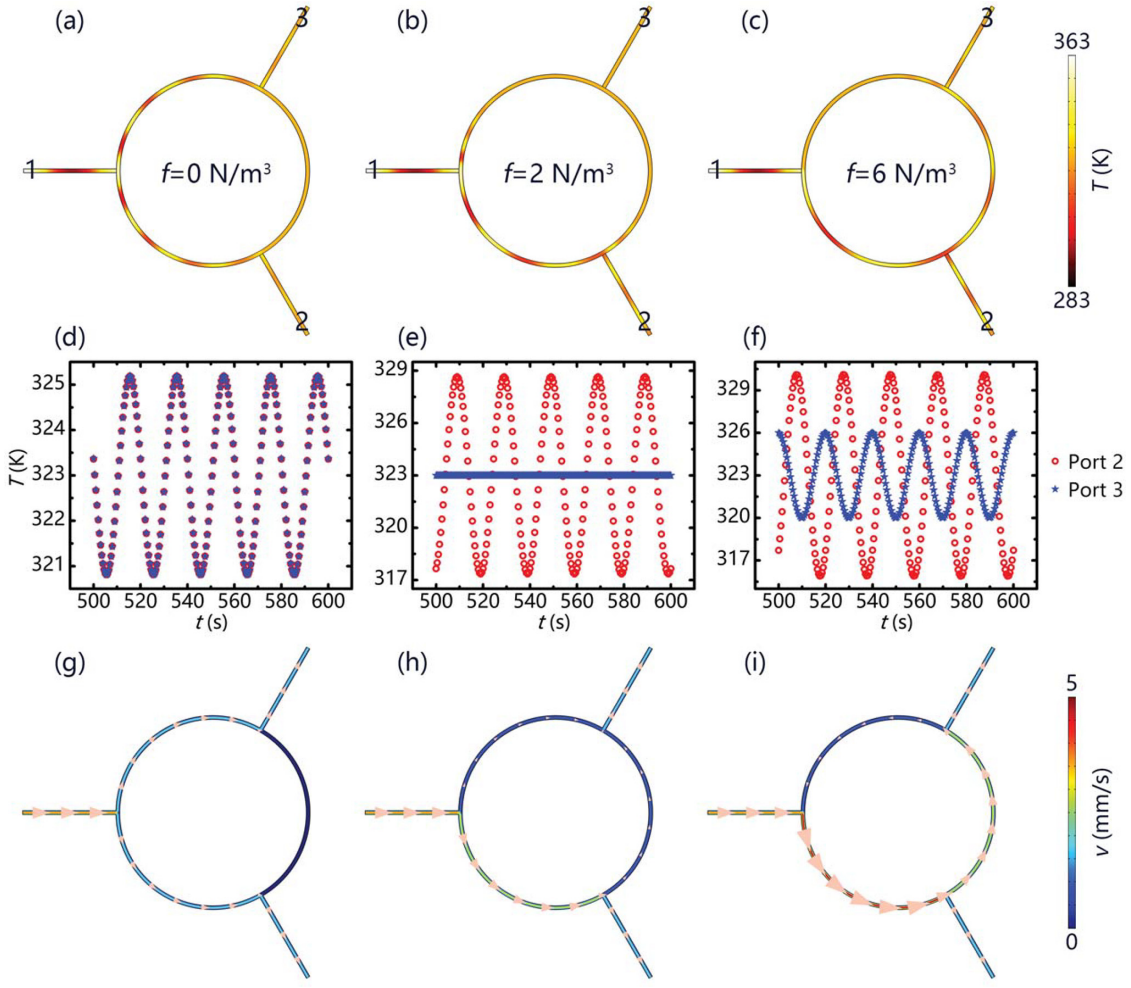

FIG. 2. Temperature and velocity profiles. (a)–(c) Temperature profiles at 600 s with volume forces of 0, 2, and 6 $\mathrm{N/m^3}$, respectively. (d)–(f) Average temperatures at ports 2 and 3 from 500 to 600 s. (g)–(i) Steady velocity profiles. Arrows denote convective velocities. The fluid is water, whose mass density, heat capacity, thermal conductivity, and dynamic viscosity are 1000 $\mathrm{kg/m^3}$, 4200 $\mathrm{J\,kg^{-1}\,K^{-1}}$, 0.6 $\mathrm{W\,m^{-1}\,K^{-1}}$, and 0.001 Pa s, respectively. The structure sizes are $r_1 = 49$ mm, $r_2 = 51$ mm, $h = r_2 - r_1 = 2$ mm, and $d = 49$ mm. Other parameters: $P_h = 1$ Pa, $P_l = 0$ Pa, and $T_1 = 40\cos(-\pi t/10) + 323$ K.

After discussing temperature and velocity properties, we are allowed to further explore heat flux properties. We independently study conductive fluxes and convective fluxes for clarity. Temperature amplitudes decay spatially $T = Ae^{-\alpha x}\cos(\beta x - \omega t) + T_0$ with α being spacial decay rate. Conductive fluxes are given by $J_{cond} = -\kappa\partial T/\partial x = \kappa A e^{-\alpha x}[\alpha\cos(\beta x - \omega t) + \beta\sin(\beta x - \omega t)]$, which are proportional to T. Convective fluxes are determined by $J_{conv} = \rho C v T$, which are also proportional to T. Therefore, heat flux properties are similar to temperature properties due to $J \propto T$. Since conductive fluxes are related to spatial derivation, we discuss heat fluxes very close to ports 2 and 3 (with a 4 mm distance) to ensure accuracy. Finite-element simulations are presented in Fig. 3. When the volume force is zero, the conductive fluxes (or convective fluxes) at ports 2 and 3 are identical (see the first column of Fig. 3). When an optimal volume force $f_{opt} = 2\,\mathrm{N/m^3}$ is applied, the conductive flux vanishes at port 3 but still exists at port 2 (like an alternating conductive flux). Therefore, the isolation of conductive fluxes is achieved. Although the convective flux at port 3 is nonzero, it does not vary temporally. The convective flux at port 2 still varies periodically (see the second column of Fig. 3). When the volume force is $6\,\mathrm{N/m^3}$, conductive and convective fluxes are also nonreciprocal (see the last column of Fig. 3).

We further discuss thermal nonreciprocity quantitatively, and six key positions Σ_1-Σ_6 are labeled in Fig. 4(a). We define two transmission coefficients as $R_{1-2} = A_2/A_1$ and $R_{1-3} = A_3/A_1$, where A_1, A_2, and A_3 are the temperature amplitudes at ports 1, 2, and 3, respectively. We also define a rectification coefficient η as $(R_{1-2} - R_{1-3})/(R_{1-2} + R_{1-3})$. R and η as a function of f are shown in Fig. 4(b1) with volume force steps of $0.1\,\mathrm{N/m^3}$. R_{1-2} first increases, then decreases, and finally varies quasiperiodically. R_{1-3} decreases initially, increases afterwards, and varies quasiperiodically at last. R_{1-2} and R_{1-3} lead to an initial increase and a final decrease in η, and $\eta_{max} = 1$ appears at $f_{opt} = 2\,\mathrm{N/m^3}$, indicating the isolation of temperature propagation at port 3. Although R_{1-2} and R_{1-3} ultimately vary quasiperiodically, they are synchronous, so η still decreases. We also change the circular frequency to $2\pi/15$ rad/s, and the transmission results are shown in Fig. 4(b2). $\eta_{max} = 1$ still appears at $f_{opt} = 2\,\mathrm{N/m^3}$. We then explain two main phenomena quantitatively, i.e., the optimal volume force f_{opt} and the final quasiperiodic variations of R_{1-2} and R_{1-3}. For clarity, we also plot the average convective velocities at positions Σ_1-Σ_6 as a function of volume force in Fig. 4(b3).

The optimal volume force f_{opt} can be quantitatively predicted by scalar (i.e., temperature) interference. Different from vector (say, electric or magnetic field) interference in wave systems, scalar interference cannot be explained by the principle of vector superposition. A key point to understand scalar interference is the decay rate. Let us take a visual example. Constructive interference refers to that a high temperature meets another high temperature, but the mixed temperature is not doubled and just decays as before. Destructive interference refers to that a high temperature meets a low temperature, and the mixed temperature decays immediately with a far larger decay rate.

We then use scalar interference to explain thermal nonreciprocity. The transmission at port 2 has only one route, i.e., Σ_1-Σ_5-Σ_2. However, the transmission at port 3 has two routes, i.e., Σ_1-Σ_5-Σ_6-Σ_3 and Σ_1-Σ_4-Σ_3. When two routes have a phase difference of $(2N_1 - 1)\pi$ with N_1 being an integer, destructive interference causes the transmission at port 3 to reach a local minimum value. To achieve a global minimum transmission at port 3, the temperature amplitudes of routes Σ_1-Σ_5-Σ_6-Σ_3 and Σ_1-Σ_4-Σ_3 should be comparable, which requires $v_{\Sigma_6} \gtrsim v_{\Sigma_4}$ ($\gtrsim$ means a little greater than). These requirements can be summarized as

$$\left[-\beta(v_{\Sigma_4}) + \beta(v_{\Sigma_5}) + \beta(v_{\Sigma_6})\right]\pi(r_1 + r_2)/3 = (2N_1 - 1)\pi, \quad (2a)$$

$$f_{opt} \gtrsim f_{v_{\Sigma_4} = v_{\Sigma_6}} = \frac{3(P_h - P_l)}{2(2\pi r_2 + 9d)}, \quad (2b)$$

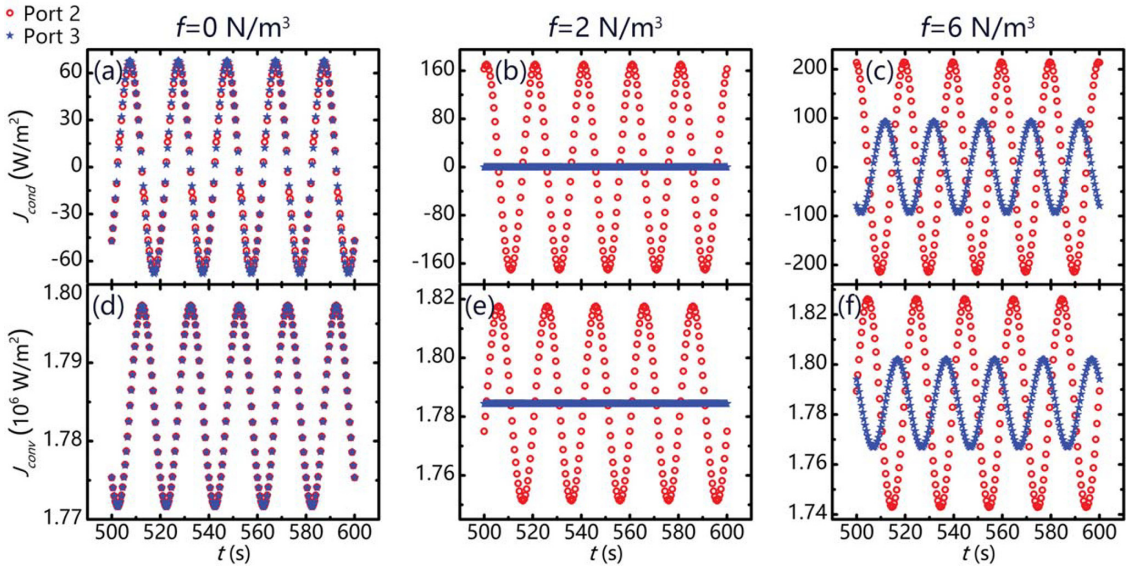

FIG. 3. Heat flux profiles. (a)–(c) Conductive fluxes and (d)–(f) convective fluxes with volume forces of 0, 2, and $6\,\mathrm{N/m^3}$, respectively. Conductive fluxes have negative values due to direction changes.

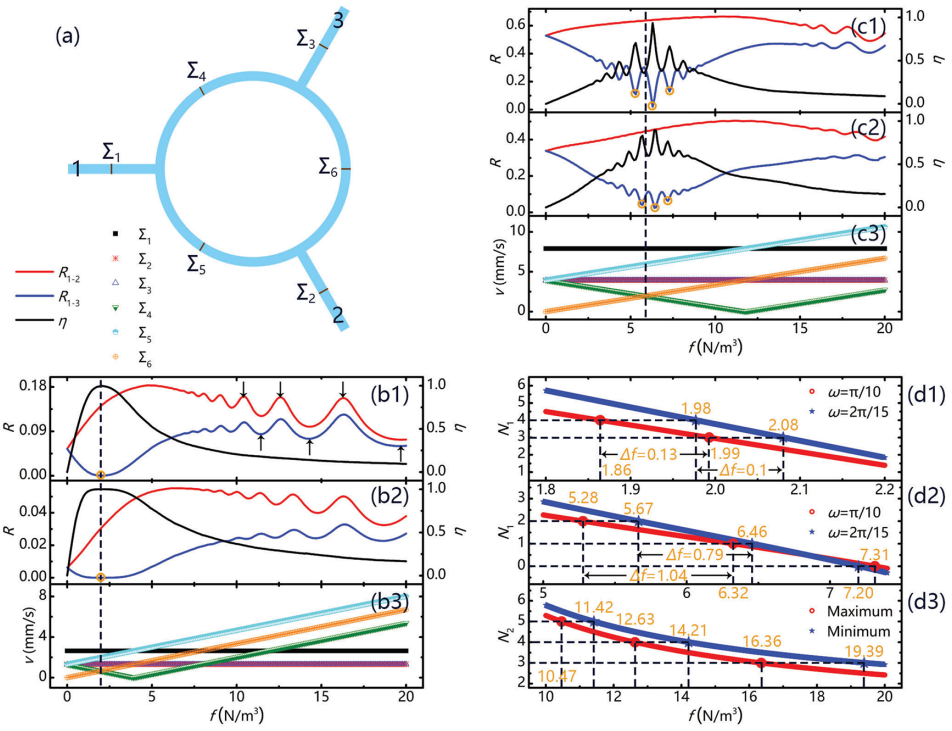

FIG. 4. Quantitative analyses of transmission coefficients and rectification coefficients. (a) Schematic diagram showing six key positions Σ_1-Σ_6. Transmission coefficient R, rectification coefficient η, and convective velocity v as a function of volume force with (b1)–(b3) $P_h = 1$ Pa and (c1)–(c3) $P_h = 3$ Pa. The circular frequencies of periodic temperature profiles are $\pi/10$ for [(b1) and (c1)] and $2\pi/15$ for [(b2) and (c2)]. The $N_1 - f$ curves described in Eq. (2a) with (d1) $P_h = 1$ Pa and (d2) $P_h = 3$ Pa. (d3) The $N_2 - f$ curves described in Eqs. (5a) and (5b).

where Eq. (2a) ensures destructive interference and Eq. (2b) ensures comparable temperature amplitudes of routes Σ_1-Σ_5-Σ_6-Σ_3 and Σ_1-Σ_4-Σ_3. The additional requirement described in Eq. (2b) also reflects the difference between convection-diffusion systems and wave systems. Since wave systems are usually Hermitian without loss, it does not require to consider wave amplitudes. However, convection-diffusion systems are non-Hermitian with loss,[19] so temperature amplitudes should be considered. The wave number β can be expressed as a function of convective velocity v

$$\beta(v) = \frac{\sqrt{-2v^2 + 2\sqrt{v^4 + 16\omega^2 D^2}}}{4D}, \tag{3}$$

where the convective velocities at positions Σ_4, Σ_5, and Σ_6 are

$$v_{\Sigma_4} = -\frac{h^2}{12\mu}\left[-\frac{3(P_h - P_l)}{2\pi r_2 + 9d} + f\right], \tag{4a}$$

$$v_{\Sigma_5} = -\frac{h^2}{12\mu}\left[-\frac{3(P_h - P_l)}{2\pi r_2 + 9d} - f\right], \tag{4b}$$

$$v_{\Sigma_6} = \frac{h^2}{12\mu} f. \tag{4c}$$

Detailed derivations of Eqs. (2)–(4) can be found in the supplementary material.

For the results in Figs. 4(b1) and 4(b2), we plot the corresponding $N_1 - f$ curves described in Eq. (2a) in Fig. 4(d1). The f corresponding to an integer N_1 is what we require. We can also derive $f_{v_{\Sigma_4}=v_{\Sigma_6}} = 1.97$ N/m^3 according to Eq. (2b). Therefore, theoretical predictions of the optimal volume force are $f_{opt} = 1.99$ N/m^3 ($N_1 = 3$) for Fig. 4(b1) and $f_{opt} = 2.08$ N/m^3 ($N_1 = 3$) for Fig. 4(b2), which agree well with $f = 2$ N/m^3 found in simulations. Moreover, only $N_1 = 3$ appears in simulations, and other values of N_1 vanish. This is because the volume force interval between two adjacent integers of N_1, i.e., $\Delta f \approx 0.1$ N/m^3 is too small to observe.

We then increase P_h to 3 Pa to observe the scalar interference at port 3, and R_{1-3} varies quasiperiodically near $f_{v_{\Sigma_4}=v_{\Sigma_6}}$ [see Figs. 4(c1) and 4(c2)]. We take the three valleys R_{1-3} in Fig. 4(c1) or Fig. 4(c2) as an example. The corresponding volume forces are 5.3, 6.3, and 7.3 N/m^3 for Fig. 4(c1), and 5.7, 6.4, and 7.2 N/m^3 for Fig. 4(c2). The theoretical predictions with Eq. (2a) are 5.28 ($N_1 = 2$), 6.32 ($N_1 = 1$), and 7.31 ($N_1 = 0$) N/m^3 for Fig. 4(c1), and 5.67 ($N_1 = 2$), 6.46 ($N_1 = 1$), and 7.20 ($N_1 = 0$) N/m^3 for Fig. 4(c2), which are clearly presented in Fig. 4(d2). We can also derive $f_{v_{\Sigma_4}=v_{\Sigma_6}} = 5.91$ N/m^3 with Eq. (2b). Therefore, $f_{opt} = 6.32$ N/m^3 and $f_{opt} = 6.46$ N/m^3 correspond to the smallest transmissions in Figs. 4(c1) and 4(c2), respectively. Meanwhile, $\eta_{max} = 0.94$ appears at $f = 6.3$ N/m^3 in Fig. 4(c1), and $\eta_{max} = 0.90$ occurs at $f = 6.4$ N/m^3 in Fig. 4(c2). Therefore, the optimal volume force f_{opt} derived from Eqs. (2a) and (2b) is in good agreement with simulations.

The final quasiperiodic variations of R_{1-2} and R_{1-3} can be attributed to the discrete modal of the ring.[19] We take the results in Fig. 4(b1) as an example. The final variations begin at approximately $f = 8$ N/m^3, and the convective velocities at positions Σ_4, Σ_5, and Σ_6 are along the counterclockwise direction. Therefore, fluids flow counterclockwise in the ring with only a velocity difference. Since the ring can only support discrete wave numbers,[19] R_{1-2} and R_{1-3} exhibit quasiperiodic variations with f. When f corresponds to an allowed (or forbidden) wave number of the ring, transmission reaches a local maximum (or minimum) value. Therefore, the volume force for a local maximum (or minimum) transmission should satisfy

$$\left[\beta(\nu_{\Sigma_4}) + \beta(\nu_{\Sigma_5}) + \beta(\nu_{\Sigma_6})\right]\pi(r_1 + r_2)/3 = 2N_2\pi, \quad (5a)$$

$$\left[\beta(\nu_{\Sigma_4}) + \beta(\nu_{\Sigma_5}) + \beta(\nu_{\Sigma_6})\right]\pi(r_1 + r_2)/3 = (2N_2 - 1)\pi, \quad (5b)$$

where N_2 is a positive integer.

We also compare theoretical predictions with finite-element simulations by taking the right three peaks of R_{1-2} and R_{1-3} in Fig. 4(b1) as an example. Their corresponding volume forces are 10.4, 12.6, and 16.3 N/m^3, respectively. The theoretical predictions given in Eq. (5a) are 10.47 ($N_2 = 5$), 12.63 ($N_2 = 4$), and 16.36 ($N_2 = 3$) N/m^3, respectively [see Fig. 4(d3)]. We also take the right three valleys of R_{1-2} and R_{1-3} in Fig. 4(b1) as another example. Their corresponding volume forces are 11.5, 14.3, and 19.6 N/m^3, respectively. The theoretical predictions given in Eq. (5b) are 11.42 ($N_2 = 5$), 14.21 ($N_2 = 4$), and 19.39 ($N_2 = 3$) N/m^3, respectively [see Fig. 4(d3)]. Therefore, the simulations still match with the theoretical predictions of Eqs. (5a) and (5b).

We finally provide some experimental suggestions for completeness. A periodic temperature can be realized by alternately using a ceramic heater and a semiconductor cooler. Ferrofluids are a good candidate to realize a volume force, which are generally composed of ferromagnetic nanoparticles with 10 nm diameter dispersed in carrier fluids.[38] Here, we may use aqueous ferrofluids containing Fe_3O_4 nanoparticles. Compared with the thermal conductivity and viscosity of water, those of aqueous ferrofluids are slightly enhanced[39] but still approximately applicable. Then we can apply an external magnetic field to guide ferromagnetic nanoparticles to move counterclockwise, so a volume force can be effectively realized. The temperatures at ports 2 and 3 can be detected by an infrared camera. Therefore, it should be possible to observe thermal nonreciprocity experimentally.

In summary, we reveal thermal nonreciprocity based on the thermal Zeeman effect, referring to the modal splitting with an angular momentum bias generated by a volume force. The maximum rectification coefficient can reach 1, so the isolation of temperature propagation is achieved at one output port. These results can be quantitatively explained by scalar interference, whose key lies in the decay rate. The proposed mechanism does not require nonlinear and phase-change materials, which has a wide range of applicability. Thermal nonreciprocity may not only have potential applications to reduce thermal fluctuation and realize thermal stabilization, but also open new directions in thermal metamaterials[40] such as topological thermotics, as schematically shown in Fig. 1(d). Moreover, an angular momentum bias is also general for other convection-diffusion systems such as mass transport,[41,42] chemical mixing,[43] and colloid aggregation,[44,45] where mass diffusivity and concentration correspond to thermal diffusivity and temperature in thermal transport, respectively.

See the supplementary material for detailed derivations of Eqs. (2)–(4).

We acknowledge financial support from the National Natural Science Foundation of China under Grant Nos. 11725521 and 12035004 and from the Science and Technology Commission of Shanghai Municipality under Grant No. 20JC1414700.

DATA AVAILABILITY

The data that support the findings of this study are available within the article and its supplementary material.

REFERENCES

[1]C. Caloz, A. Alù, S. Tretyakov, D. Sounas, K. Achouri, and Z.-L. Deck-Léger, Phys. Rev. Appl. **10**, 047001 (2018).
[2]H. Nassar, B. Yousefzadeh, R. Fleury, M. Ruzzene, A. Alù, C. Daraio, A. N. Norris, G. L. Huang, and M. R. Haberman, Nat. Rev. Mater. **5**, 667 (2020).
[3]R. Fleury, D. L. Sounas, C. F. Sieck, M. R. Haberman, and A. Alù, Science **343**, 516 (2014).
[4]X. X. Liu, X. B. Cai, Q. Q. Guo, and J. Yang, New J. Phys. **21**, 053001 (2019).
[5]C. He, M.-H. Lu, X. Heng, L. Feng, and Y.-F. Chen, Phys. Rev. B **83**, 075117 (2011).
[6]J. Lian, J.-X. Fu, L. Gan, and Z.-Y. Li, Phys. Rev. B **85**, 125108 (2012).
[7]D. L. Sounas, C. Caloz, and A. Alù, Nat. Commun. **4**, 2407 (2013).
[8]D. L. Sounas and A. Alù, ACS Photonics **1**, 198 (2014).
[9]R. Fleury, D. L. Sounas, and A. Alù, Phys. Rev. B **91**, 174306 (2015).
[10]Y. F. Wang, B. Yousefzadeh, H. Chen, H. Nassar, G. L. Huang, and C. Daraio, Phys. Rev. Lett. **121**, 194301 (2018).
[11]M. Y. Wong, C. Y. Tso, T. C. Ho, and H. H. Lee, Int. J. Heat Mass Transfer **164**, 120607 (2021).
[12]Y. Li, X. Y. Shen, Z. H. Wu, J. Y. Huang, Y. X. Chen, Y. S. Ni, and J. P. Huang, Phys. Rev. Lett. **115**, 195503 (2015).
[13]T. J. Alexander, Phys. Rev. E **101**, 062122 (2020).
[14]Y. Li, J. X. Li, M. H. Qi, C.-W. Qiu, and H. S. Chen, Phys. Rev. B **103**, 014307 (2021).
[15]D. Torrent, O. Poncelet, and J.-C. Batsale, Phys. Rev. Lett. **120**, 125501 (2018).
[16]L. J. Xu, J. P. Huang, and X. P. Ouyang, Phys. Rev. E **103**, 032128 (2021).
[17]M. Farhat, S. Guenneau, P.-Y. Chen, A. Alù, and K. N. Salama, Phys. Rev. Appl. **11**, 044089 (2019).
[18]M. Gandolfi, C. Giannetti, and F. Banfi, Phys. Rev. Lett. **125**, 265901 (2020).
[19]Y. Li, Y.-G. Peng, L. Han, M.-A. Miri, W. Li, M. Xiao, X.-F. Zhu, J. L. Zhao, A. Alù, S. H. Fan, and C.-W. Qiu, Science **364**, 170 (2019).
[20]P. C. Cao, Y. Li, Y. G. Peng, C. W. Qiu, and X. F. Zhu, ES Energy Environ. **7**, 48 (2020).
[21]L. J. Xu, J. Wang, G. L. Dai, S. Yang, F. B. Yang, G. Wang, and J. P. Huang, Int. J. Heat Mass Transfer **165**, 120659 (2021).
[22]L. J. Xu and J. P. Huang, Int. J. Heat Mass Transfer **159**, 120133 (2020).
[23]L. J. Xu and J. P. Huang, Appl. Phys. Lett. **117**, 011905 (2020).
[24]L. J. Xu and J. P. Huang, Chin. Phys. Lett. **37**, 080502 (2020).
[25]L. J. Xu and J. P. Huang, Chin. Phys. Lett. **37**, 120501 (2020).
[26]A. B. Khanikaev, R. Fleury, S. H. Mousavi, and A. Alù, Nat. Commun. **6**, 8260 (2015).
[27]X. Ni, C. He, X.-C. Sun, X.-P. Liu, M.-H. Lu, L. Feng, and Y.-F. Chen, New J. Phys. **17**, 053016 (2015).
[28]R. Fleury, A. B. Khanikaev, and A. Alù, Nat. Commun. **7**, 11744 (2016).
[29]Y. J. Ding, Y. G. Peng, Y. F. Zhu, X. D. Fan, J. Yang, B. Liang, X. F. Zhu, X. G. Wan, and J. C. Chen, Phys. Rev. Lett. **122**, 014302 (2019).
[30]X. X. Liu, Q. Q. Guo, and J. Yang, Appl. Phys. Lett. **114**, 054102 (2019).
[31]X. X. Liu, Q. Q. Guo, and J. Yang, Appl. Phys. Lett. **115**, 074102 (2019).
[32]J. P. Huang, *Theoretical Thermotics: Transformation Thermotics and Extended Theories for Thermal Metamaterials* (Springer, Singapore, 2020).
[33]G. L. Dai, J. Shang, and J. P. Huang, Phys. Rev. E **97**, 022129 (2018).
[34]J. Park, J. R. Youn, and Y. S. Song, Phys. Rev. Lett. **123**, 074502 (2019).
[35]J. Park, J. R. Youn, and Y. S. Song, Phys. Rev. Appl. **12**, 061002 (2019).
[36]W.-S. Yeung, V.-P. Mai, and R.-J. Yang, Phys. Rev. Appl. **13**, 064030 (2020).
[37]G. K. Batchelor, *An Introduction to Fluid Dynamics* (Cambridge University Press, 2000).
[38]S. Odenbach, *Magnetoviscous Effects in Ferrofluids* (Springer, Berlin, 2002).
[39]P. D. Shima, J. Philip, and B. Raj, Appl. Phys. Lett. **95**, 133112 (2009).
[40]J. Wang, G. L. Dai, and J. P. Huang, iScience **23**, 101637 (2020).
[41]J. M. Restrepo-Florez and M. Maldovan, Appl. Phys. Lett. **111**, 071903 (2017).
[42]L. J. Xu, G. L. Dai, G. Wang, and J. P. Huang, Phys. Rev. E **102**, 032140 (2020).
[43]F. Avanzini, G. Falasco, and M. Esposito, Phys. Rev. E **101**, 060102 (2020).
[44]A. Zaccone, H. Wu, D. Gentili, and M. Morbidelli, Phys. Rev. E **80**, 051404 (2009).
[45]L. Banetta and A. Zaccone, Phys. Rev. E **99**, 052606 (2019).